

A nickel–manganese catalyst as a biomimic of the active site of NiFe hydrogenases: a combined electrocatalytical and DFT mechanistic study†

Vincent Fourmond,^a Sigolène Canaguier,^a Benjamin Golly,^b Martin J. Field,^b Marc Fontecave^{ac} and Vincent Artero^{*a}

Received 2nd December 2010, Accepted 11th January 2011

DOI: 10.1039/c0ee00736f

The dinuclear nickel–manganese complex $[\text{Ni}(\text{xbsms})\text{Mn}(\text{CO})_3(\text{H}_2\text{O})]^+$ (H_2xbsms = 1,2-bis-(4-mercapto-3,3-dimethyl-2-thiabutyl)benzene) is reported as a bio-inspired mimic of the active site of NiFe hydrogenases catalyzing hydrogen evolution from trifluoroacetic acid in DMF with an overpotential requirement of 860 mV. This is higher than that displayed by Ni–Ru systems [Canaguier *et al.*, *Chem.–Eur. J.*, 2009, **15**, 9350–9364] but similar to that found for related noble metal free Ni–Fe mimics [Canaguier *et al.*, *Chem. Commun.* 2010, **46**, 5876–5878]. A combined electrochemical and theoretical (DFT) study suggests a heterolytic mechanism for hydrogen evolution from a hydride derivative. The structure of the active intermediate, with a bridging hydride ligand between Ni and Mn, resembles that of the Ni–C active state of NiFe hydrogenases.

1. Introduction

Of the technological solutions developed for hydrogen/water interconversion, proton-exchange-membrane fuel-cells and electrolyzers appear the most promising due to their high yield and compactness.¹ However, these approaches rely on the properties of platinum, which is a scarce and expensive metal, for catalytic hydrogen evolution or uptake. If water conversion

technologies are to become economically viable, replacement of platinum by lower cost and more abundant materials is a prerequisite.²

Hydrogenases are enzymes that efficiently catalyze such reactions using only iron and nickel metal centres.³ Thus, a promising route to the replacement of Pt in cells for H_2 production or oxidation is to employ bio-inspired synthetic catalysts that contain these more readily available metals. Such catalysts are easy to prepare and can often be handled in air, which is key for their integration in a technological device. A definitive proof of the relevance of this biomimetic approach appeared very recently from our group.^{4–6} We showed that covalent attachment of a mimic of the active sites of hydrogenases onto carbon nanotubes produces an efficient electrocatalytic nanomaterial for hydrogen production and uptake, at vanishingly low overpotential and with outstanding stability. Obviously, the exceptional properties of such a material are a consequence of the exquisite bio-inspired design of the molecular catalyst.^{7–10}

^aLaboratoire de Chimie et Biologie des Métaux, Université Joseph Fourier, CNRS UMR 5249, CEA, DSV/IRTSV, 17 rue des Martyrs, F-38054 Grenoble Cedex 9, France. E-mail: vincent.artero@cea.fr; Fax: +33 438789124; Tel: +33 438789106

^bLaboratoire de Dynamique moléculaire, Institut de Biologie Structurale, “Jean-Pierre Ebel”, UMR CNRS/UJF/CEA 5075, 41 rue Jules Horowitz, F-38027 Grenoble cedex 1, France. E-mail: martin.field@ibs.fr; Fax: +33 438785122; Tel: +33 438785904

^cCollège de France, 11 place Marcellin-Berthelot, F-75005 Paris

† Electronic supplementary information (ESI) available. See DOI: 10.1039/c0ee00736f

Broader context

The future of energy supply depends on innovative breakthroughs regarding the design of cheap, sustainable and efficient systems for the conversion and storage of renewable energy sources, such as wind and solar energy. The production of hydrogen, a fuel with remarkable properties, through water splitting appears as a promising and appealing solution. Electro-catalysis is a key enabling technology in this context since the requirement for noble metal-based catalysts (Pt, IrO_2 , ...) is the main limitation for electrolysis and fuel-cell technologies to become economically viable. Nature is an inspiration for the design of alternative catalysts employing abundantly occurring elements since the active sites of enzymes that are involved in the water-splitting process in natural systems, namely hydrogenases and photosystem II, use iron, nickel and manganese ions for catalysis. Imitating the active site of an enzyme in the form of a small synthetic chemical material allows one to produce cheap and robust catalysts that may be further implemented in technological devices.

Improvement of the properties of this material in terms of current density requires an increase in the intrinsic turnover frequency of the grafted catalyst which in turn relies on further development of bio-inspired hydrogenase mimics.

In contrast to the development of mimics of the active site of FeFe hydrogenases (Fig. 1) numbering hundreds of papers in the literature^{11,12} major achievements remain to be made if the catalytic activity of NiFe hydrogenases is to be reproduced.¹³ Despite the synthesis of more than 50 structural mimics of their active sites (Fig. 1), there are few nickel-based dinuclear complexes that are catalytically competent for H⁺/H₂ interconversion. These include a series in which Ru replaces Fe, described by the group of Ogo¹⁴ for H₂ oxidation and by our group for H₂ evolution,^{15–17} and a small number of Ni–Fe complexes.^{18–20}

The low-spin d⁶ *fac*-{Mn(CO)₃}⁺ cyanthrene fragment is both isolobal and isoelectronic with the d⁶ *fac*-{Fe(CO)(CN)₂} motif found at the active site of NiFe hydrogenase.²¹ We report that combining such an organometallic moiety with a nickel centre in a sulfur rich environment yields a robust electro-catalyst (Fig. 2) for hydrogen evolution from trifluoroacetic acid in DMF. A detailed electrochemical study coupled with electrokinetic simulations and quantum chemical calculations suggests that the hydrogen evolution catalyzed by this new Ni–Mn biomimic proceeds through the protonation of a hydride intermediate with a bridging {Ni(μ-H)Mn} structure similar to the catalytically competent Ni–C form of NiFe hydrogenases. Such a heterolytic H₂ evolution route likely parallels the biological process found in native hydrogenases.

2. Results

2.1 Synthesis

Reaction of [Ni(xbsms)]²² (H₂xbsms = 1,2-bis(4-mercapto-3,3-dimethyl-2-thiabutyl)benzene) with [Mn(CO)₅Br] in deaerated diethyl ether yields an insoluble material analyzed as [Ni(xbsms)Mn(CO)₃(H₂O)]Br (**1Br**, Fig. 2). Electrospray ionisation mass spectrometry (ESI-MS) confirms the presence of a dinuclear {Ni(xbsms)Mn(CO)₃}⁺ butterfly core (*m/z* = 541) with two thiolate ligands bridging the Mn and Ni centres. Use of other precursors for the {Mn(CO)₃}⁺ fragments such as [Mn(CO)₃(acetone)₃](Otf), [Mn(CO)₃(acetone)₃](BF₄) and [Mn(CO)₃(OH)₂](BF₄) in CH₂Cl₂ or CH₂Cl₂/aqueous acetate buffer²³ yields compounds with similar IR, ¹H NMR and ESI-MS signatures, thus confirming the absence of any Mn-coordinated anionic ligand. Because the chemistry of {Mn^I(CO)₃} compounds is dominated by electronically saturated 18-electron

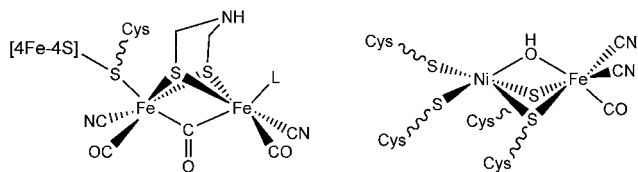


Fig. 1 Structure of the active sites of FeFe hydrogenases in the oxidized state (left, L = OH₂ or OH[−]) and NiFe hydrogenases in the Ni–B inactive ready state (right, the oxygenated bridging ligand is not present in the reduced active states).

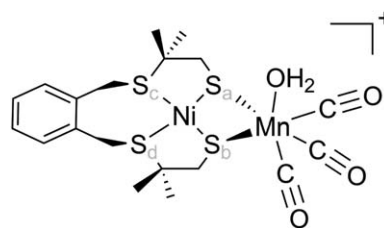


Fig. 2 Structure of the [Ni(xbsms)Mn(CO)₃(H₂O)]⁺ (**1**⁺) cation.

complexes,²⁴ we favor labile coordination of a water molecule as a sixth ligand of the Mn center.²⁵

2.2 Spectroscopic characterization

The infrared spectrum of **1Br** (CH₂Cl₂ solution) displays 3 CO-stretching absorption bands at 2018 (vs), 1929 (m, br) and 1911 cm^{−1}. By comparison with the A₁ + E pattern typical for *fac*-tricarbonyl coordination in octahedral complexes, the splitting of the E band observed in both the solution and solid state spectra²³ indicates some loss of symmetry due to the mixed set of thiolate and aqua ligands.

As expected for a structure with C_s symmetry and heterotopic faces typical of those for similar dinuclear complexes,^{15,17,18,26,27} the room temperature ¹H NMR spectrum of **1Br** in CD₂Cl₂ displays two singlets for the methyl groups and four doublets corresponding to two AB systems for the benzylic and methylenic protons of the xbsms^{2−} ligand. Attempts to grow monocrystals suitable for X-ray diffraction studies systematically resulted in CO loss and generation of oligomeric Ni–Mn complexes.²⁸ Dinuclear complexes with {Ni(xbsms)M} butterfly cores (M = Fe,¹⁸ Ru^{15,17,26,27}) and without M-coordinated bulky ligands belong to two structural types depending on whether the aromatic cycle of the xbsms^{2−} ligand is in *cis* (class I) or *trans* (class III) configuration with respect to the NiS₄ plane.¹⁷ The structures and energies of both class I and class III isomers of **1**⁺ (Fig. 3) were optimized using DFT quantum chemical methods in DMF (see Experimental section). Computations using the B3LYP and BP86 functionals give similar energies for the class I and class III isomers within the accuracy of the method. In the following study, and for the sake of clarity, we show only the class III isomeric structures since these are fractionally more stable (between 6 and 15 kJ mol^{−1}) throughout the catalytic cycle. Nevertheless, the conclusions that we draw about the catalysis apply to both isomer classes. Structural parameters computed for **1**⁺ are shown in Table 1.

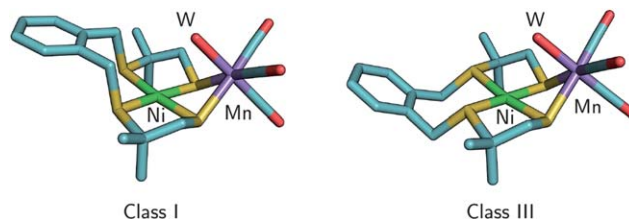


Fig. 3 Structures for the class I (left) and III (right) isomeric structures considered for **1**⁺. The class III isomer is slightly more stable from the DFT calculations and is the one that is presented throughout the article. W stands for a water molecule.

Table 1 DFT (BP86/LACV3P**++) in DMF optimized structural data for the species in the H₂-evolving catalytic cycles of the class III isomer of **1**⁺ (see Table S1† for results obtained with the B3LYP functional). Of the three CO ligands, two occupy equivalent environments and show very similar and often identical properties. Their (average) values are shown first in the CO rows.

Bond/angle	1 ⁺	[NiMn]	[NiMn] [−]	[NiHMn]	[Ni(H ₂)Mn] ⁺	[NiMn] ⁺	[NiHMn] [−]	[Ni(H ₂)Mn]
Ni–Mn	3.152	2.860	2.769	2.749	2.950	2.792	2.675	2.851
Mn–OH ₂	2.162							
Mn–H				1.632	1.762, 1.801		1.661	1.733, 1.840
Ni–H				1.930	2.122, 2.940		1.762	1.874, 2.727
Ni–H–Mn				100.7			102.7	
Mn–CO _{average}	1.786, 1.786	1.771, 1.794	1.763, 1.777	1.766, 1.808	1.796, 1.791	1.792, 1.764	1.760, 1.791	1.784, 1.791
Ni–Mn–CO	128.2, 115.5	111.1, 140.6	111.1, 140.1	115.9, 134.4	125.2, 121.4	115.6, 140.5	115.1, 134.9	125.2, 120.6
Hinge Ni–2S–Mn	123.2	108.9	103.1	100.0	110.4	106.8	95.8	103.7
Hinge 2S–Ni–2S	170.7	173.4	174.0	178.4	171.6	172.8	176.4	172.7

2.3 Electrochemical characterization

The cyclic voltammogram of **1Br** recorded in DMF at 100 mV s^{−1} (red trace in Fig. 4; see also Fig. S1†) displays two reductive waves at −1.53 and −1.83 V vs. Fc⁺/Fc. Their irreversible nature indicates that electron transfer is immediately followed by a fast chemical reaction or structural rearrangement. We could not outrun follow-up reactions at the highest scan rate of 30 V s^{−1}, which sets a lower limit upon their rate constants *k* of about $F\nu/RT = 10^3$ s^{−1} (with *F* the Faraday constant and ν the maximum scan rate). Assuming that these reactions do not proceed with a rate faster than 10⁹ s^{−1} and using eqn (1), which gives the peak potential of a one-electron reduction followed by an irreversible chemical reaction,²⁹ the redox potentials of the first and second reductions of the complex are found to be within the following ranges: −1.81 < *E*₁⁰ < −1.61 V vs. Fc⁺/Fc and −2.11 < *E*₂⁰ < −1.93 V vs. Fc⁺/Fc. Additionally, fitting the current of the peaks to eqn (2) (*A* is the surface of the electrode) gives a diffusion coefficient for **1Br** of *D* = 1.1 ± 0.1 · 10⁶ cm² s^{−1}.

$$E_p = E_{1/2} - \frac{RT}{F} \times \left[0.780 - \ln \sqrt{RTk/F\nu} \right] \quad (1)$$

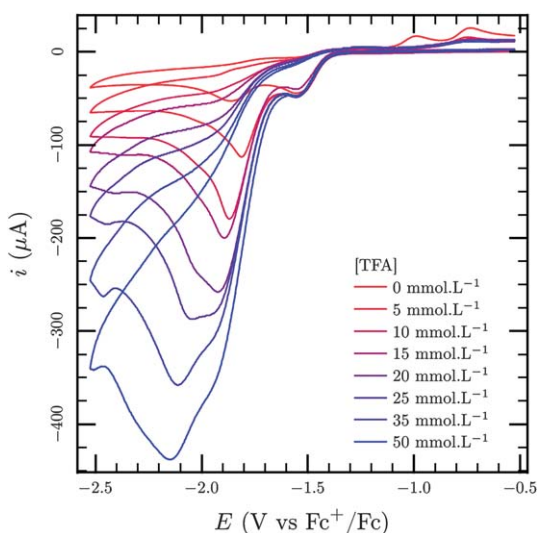


Fig. 4 Cyclic voltammograms of **1Br** (5.0 mmol L^{−1}) in the presence of various concentrations of trifluoroacetic acid (TFA) recorded in a DMF solution of *n*-Bu₄NBF₄ (0.1 mol L^{−1}) on a glassy carbon electrode at 100 mV s^{−1}.

$$i_p/[C] = 0.496 \times FA\sqrt{D} \times \sqrt{F\nu/RT} \quad (2)$$

2.4 Electrocatalytic hydrogen evolution

Upon addition of trifluoroacetic acid (TFA) to an electrolytic solution of **1Br**, a large irreversible wave appears after the first reduction wave and grows upon the second one in the cyclic voltammogram. For acid concentrations above a ~5-fold excess of the catalyst concentration, a second catalytic wave appears at slightly more negative potentials. From blank voltammograms recorded in the absence of **1Br**, we can assign this second catalytic process to the direct reduction of the acid at the glassy-carbon electrode. No catalytic wave was observed in the presence of the weaker acid triethylammonium.

To confirm that this wave corresponds to the catalytic reduction of TFA into H₂, we performed a bulk electrolysis experiment of a TFA (0.1 mol L^{−1}) solution in DMF (7 mL) at a constant potential (−1.82 V vs. Fc⁺/Fc) in the presence of **1Br** (1 mmol L^{−1}). During a 4 h experiment, 21.4 C flowed through the electrode and a volume of 2.5 mL H₂ gas evolved. This gives a Faradaic yield of 94% and a turnover number of 15.8 for an average turnover frequency of about 4 per hour.

Following the electrochemical method we recently proposed,³⁰ we determined a p*K*_a value of 6.0 (±0.3) for TFA in DMF (see ESI†). From this value, a theoretical half-wave potential value for the reduction of TFA (10 mmol L^{−1}) in DMF of −950 mV vs. Fc⁺/Fc can be obtained. We measured a half-wave potential of −1.81 V vs. Fc⁺/Fc for the catalytic wave under similar conditions, thus giving an overpotential requirement of 860 mV for H₂ evolution catalyzed by **1Br**.

2.5 Mechanistic studies

In this section, a systematic study of the dependence of the catalytic cyclic voltammograms, such as those of Fig. 4, on scan rate and acid and catalyst concentrations is reported together with DFT modelling results to clarify the mechanism for H₂ evolution catalyzed by **1Br**. We assume that a dinuclear Ni–Mn species is the active one because we can exclude metal nanoparticles,³¹ since the catalytic activity is retained on a mercury pool, and mononuclear complexes derived from dissociation of the dinuclear complex, since [Ni(xbsms)] and {Mn(CO)₃} species are very poorly active.^{18,32}

The absence of modification of the first wave upon addition of TFA indicates that the one-electron reduced compound $[\text{NiMn}]$ is not basic enough to be protonated. By contrast, the catalytic wave grows on top of the second reduction wave of **1Br**, strongly suggesting that the catalytic mechanism involves the protonation of the double-reduced state yielding a hydride species $[\text{NiHMn}]$ (Fig. 5). From this species, two general routes can be considered for the formation of molecular hydrogen. The so-called homolytic pathway, in which the hydrogen molecule is formed by a bimolecular reductive elimination reaction of two hydride complexes, and a heterolytic pathway that involves further protonation of the hydride to form H_2 (Fig. 5). Homolytic and heterolytic hydrogen evolution may also proceed from a reduced, and thereby activated, hydride derivative $[\text{NiHMn}]^-$ produced at the electrode (Fig. 5).

In the following sections, we first discuss DFT modelling of the catalytic pathways shown in Fig. 5, and then simulations of the catalytic behaviours of the homolytic and heterolytic mechanisms. Together the results of these two complementary techniques allow a precise picture to be built up of the individual steps in the catalytic reduction of TFA to hydrogen.

2.5.1 DFT modelling. Starting from an optimized structure of **1**⁺, DFT modelling was first carried out with both B3LYP and BP86 functionals, to characterize the two reduction processes observed in the absence of acid. Computations of the energies (Table 2) of the one-electron reduced compounds $[\text{Ni}(\text{xbsms})\text{Mn}(\text{CO})_3(\text{H}_2\text{O})]$ (**1**) and $[\text{Ni}(\text{xbsms})\text{Mn}(\text{CO})_3]$ (thereafter abbreviated as $[\text{NiMn}]$, Table 1) indicate entropy-driven favorable elimination of water from the Mn coordination sphere. Thus the irreversibility of the first reduction process can be assigned to the elimination of the Mn-coordinated water molecule following reduction (Fig. 5). From charge and spin analyses, reduction initially yields a $\text{Ni}^{\text{I}}\text{Mn}^{\text{I}}$ species that rearranges into a $\text{Ni}^{\text{II}}\text{Mn}^0$ species after elimination of the water ligand (Tables 3 and 4). As for the second reduction wave, spin and charge analyses of $[\text{Ni}(\text{xbsms})\text{Mn}(\text{CO})_3]^-$ ($[\text{NiMn}]^-$) suggest a $\text{Ni}^{\text{I}}\text{Mn}^0$ electronic structure with strong charge delocalisation onto the Ni-bound sulfur atoms. The bond orders of the Ni–S bonds are also significantly lessened, by an average 0.25 (Table 5). We have previously shown that interconversion between the class I and class III isomers requires the consecutive cleavage of two Ni–S_{thioether} bonds.¹⁷ The barrier for this process is likely to be quite low in this two-electron reduced state, due to the weaker Ni–S bonds so that isomerisation may be responsible for electrochemical irreversibility.³³ No elimination of CO ligand was observed in any of our calculations of the one and two-electron

reduced species as the Mn–CO bond orders remained slightly above unity in all redox states, regardless of the functional used.

Electrochemical potentials of the first reduction step determined by DFT are in the range of E_1^0 values obtained by analyzing the electrochemical traces. It is less satisfactory, but still within acceptable accuracy,³⁴ for the second reduction potential E_2^0 .

Next we computed the structures (Fig. 6) and energies (Table 2) of all the intermediates involved in the catalytic pathways shown in Fig. 5. Structural and electronic data for these intermediates are given in Tables 1, 3, 4 and 5. We first investigated protonation of $[\text{NiMn}]^-$ and found a bridging hydride structure $[\text{NiHMn}]$ (Fig. 6) with a Ni–H–Mn angle of 100.7° and an Ni–H bond length (1.93 Å) that is significantly larger than the Mn–H distance (1.63 Å). Reduction of $[\text{NiHMn}]$ yields $[\text{NiHMn}]^-$ with a bridging structure in which the Ni–H distance shortens significantly (from 1.93 to 1.76 Å) and the Mn–H bond length (from 1.63 to 1.61 Å) remains unchanged (Table 1 and Fig. 6).

Bimolecular steps involving either two $[\text{NiHMn}]$ or two $[\text{NiHMn}]^-$ species are calculated as uphill processes with endothermicities of between 60 and 90 kJ mol^{−1} (Table 2). From DFT computations, we can therefore exclude that catalysis proceeds through a homolytic mechanism.

From $[\text{NiHMn}]$, the heterolytic route first requires a protonation step yielding a dihydrogen complex $[\text{Ni}(\text{H}_2)\text{Mn}]^+$. The resulting H_2 molecule, with a H–H bond length of 0.84 Å, is coordinated side-on to Mn with the Ni, Mn and two H atoms being coplanar (Fig. 6). The Mn–H distances are in the range 1.73–1.84 Å and one Ni–H distance is quite short (1.87–2.05 Å), resulting in a dissymmetric H–H bond. Both structures correspond to true dihydrogen complexes since the H–H bond lengths are shorter than 1.0 Å.³⁵ The interaction of the dihydrogen ligand with the Ni centre is also confirmed by the Mayer bond orders. This dihydrogen complex shows very weak binding (Table 2) so that liberation of H_2 is entropically possible, yielding $[\text{NiMn}]^+$ similar to **1**⁺ but lacking the water molecule coordinated to the Mn centre.

A second heterolytic pathway starts from $[\text{NiHMn}]^-$. The calculated reduction potential of the $[\text{NiHMn}]/[\text{NiHMn}]^-$ couple is very close to that of the $[\text{NiMn}]/[\text{NiMn}]^-$ couple, and this is required from an electrochemical point of view if the second heterolytic pathway is to occur. Protonation of $[\text{NiHMn}]^-$ yields the dinuclear complex $[\text{Ni}(\text{H}_2)\text{Mn}]$ (Fig. 6) with structural features similar to $[\text{Ni}(\text{H}_2)\text{Mn}]^+$ except for a wider hinge angle at the dithiolate bridge (110.4° instead of 103.7° , Table 1). In this complex, H_2 coordination is stronger than in $[\text{Ni}(\text{H}_2)\text{Mn}]^+$ (Table 2) but liberation of dihydrogen is still possible when the entropic correction is added to the reaction energy.

Although both pathways are possible, protonation of $[\text{NiHMn}]$ is much less energetically favorable than that of $[\text{NiHMn}]^-$ and, in addition, electrochemical processes are generally fast whereas protonations of metal centres and hydride species are much slower.^{36,37} We thus consider the second route, in which reduction of $[\text{NiHMn}]$ is driven by a protonation with a high driving force, more likely than the first, in which there is direct protonation of $[\text{NiHMn}]$.

2.5.2 Electrokinetic simulations of the catalytic mechanism. Rather than trying to accurately reproduce all the features of

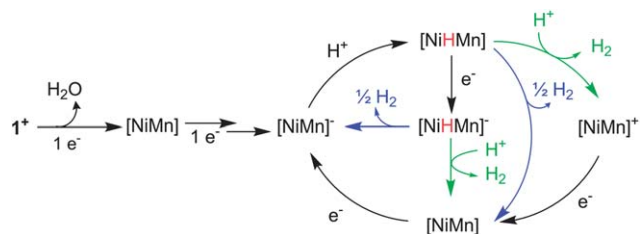


Fig. 5 Proposed electrocatalytic pathways for hydrogen evolution catalyzed by **1Br**. The homolytic H_2 -evolution steps are depicted in blue and the heterolytic steps in green.

Table 2 DFT-calculated reaction energies using both the BP86 and B3LYP functionals. AH stands for trifluoroacetic acid. The entropic contribution to the free energy of a reaction that results in a net increase of molecule number (by, for example, release of H₂ or water) has been estimated to be about 40 kJ mol^{−1} per liberated molecule.³⁸ [NiMn][−] stands for the species immediately formed after reduction of **1** and before the structural rearrangement that makes the electrochemical process irreversible

Reaction	BP86	B3LYP
1 ⁺ / 1	−1.57 V vs. Fc ⁺ /Fc	−1.43 V vs. Fc ⁺ /Fc
[NiMn]/[NiMn] [−]	−1.86 V vs. Fc ⁺ /Fc	−1.61 V vs. Fc ⁺ /Fc
[NiMn] [•] /[NiMn]	−1.38 V vs. Fc ⁺ /Fc	−1.48 V vs. Fc ⁺ /Fc
[NiHMn]/[NiHMn] [−]	−1.79 V vs. Fc ⁺ /Fc	−1.64 V vs. Fc ⁺ /Fc
1 → [NiMn] + H ₂ O	2.7 kJ mol ^{−1}	34.7 kJ mol ^{−1}
[NiMn] + AH → [NiHMn] ⁺ + A [−]	−9.8 kJ mol ^{−1}	−4.5 kJ mol ^{−1}
[NiMn] [−] + AH → [NiHMn] + A [−]	−131.8 kJ mol ^{−1}	−109.0 kJ mol ^{−1}
[NiHMn] + AH → [Ni(H ₂)Mn] ⁺ + A [−]	−18.4 kJ mol ^{−1}	−38.4 kJ mol ^{−1}
[NiHMn] [−] + AH → [Ni(H ₂)Mn] + A [−]	−56.5 kJ mol ^{−1}	−80.7 kJ mol ^{−1}
[Ni(H ₂)Mn] ⁺ → [NiMn] ⁺ + H ₂	−5.0 kJ mol ^{−1}	14.7 kJ mol ^{−1}
[Ni(H ₂)Mn] → [NiMn] + H ₂	16.1 kJ mol ^{−1}	41.5 kJ mol ^{−1}
2 [NiHMn] → 2 [NiMn] + H ₂	84.9 kJ mol ^{−1}	72.6 kJ mol ^{−1}
2 [NiMnH] [−] → 2 [NiMn] [−] + H ₂	97.9 kJ mol ^{−1}	67.0 kJ mol ^{−1}

Table 3 Mulliken spin densities for the intermediate species in the H₂-evolving catalytic cycle of **1**⁺ (class III isomers; BP86 in DMF; see Table S2† for results obtained with the B3LYP functional). Only structures with non-zero spin densities are shown

Atom	[NiMn]	[NiMn] [−]	[NiHMn] [−]	[NiMnH ₂]
Mn	0.709	0.685	−0.011	−0.021
Ni	0.072	−0.461	0.660	0.647
S _{ab}	0.008	−0.116	0.113	0.109
S _{cd}	0.014	−0.071	0.065	0.079

individual voltammograms recorded under various conditions, we found it easier to focus on the catalytic efficiency η ^{39–41} and its dependence on acid and catalyst concentrations. The catalytic efficiency η is defined as the ratio i_{cat}/i_0 , where i_{cat} is the amplitude of the catalytic wave at a given scan rate, acid and catalyst concentration, and i_0 is the amplitude of a monoelectronic reduction wave⁴² for the same scan rate and catalyst concentration, recorded in the absence of acid. Thus, the higher the catalytic efficiency, the higher the overall catalytic rate.

Table 4 Atomic (ESP) charges for the intermediate species in the H₂-evolving catalytic cycle of **1**⁺ (class III isomers; BP86 in DMF; see Table S3† for results obtained with the B3LYP functional)

Center	1 ⁺	[NiMn]	[NiMn] [−]	[NiHMn]	[Ni(H ₂)Mn] ⁺	[NiMn] ⁺	[NiHMn] [−]	[Ni(H ₂)Mn]
Mn	0.236	−0.197	−0.117	−0.044	0.014	0.115	0.194	−0.023
Ni	0.282	0.263	0.327	0.192	0.274	0.329	0.301	0.329
Water	0.118							
H				−0.226	−0.059, 0.138		−0.319	−0.013, 0.055
Total H					0.080			0.042
S _{ab}	−0.310	−0.305	−0.509	−0.266	−0.263	−0.245	−0.507	−0.427
S _{cd}	−0.105	−0.191	−0.296	−0.076	−0.107	−0.206	−0.184	−0.203
Total S	−0.829	−0.990	−1.608	−0.683	−0.739	−0.903	−1.382	−1.260
CO	−0.052, −0.014	−0.166, −0.059	−0.229, −0.136	−0.104, −0.080	−0.031, 0.085	−0.059, 0.051	−0.203, −0.179	−0.063, 0.041
Total CO	−0.118	−0.390	−0.592	−0.288	0.024	−0.067	−0.584	−0.085

Table 5 Mayer bond orders for the intermediate species in the H₂-evolving catalytic cycle of **1**⁺ (class III isomers; BP86 in DMF; see Table S4† for results obtained with the B3LYP functional)

Bond	1 ⁺	[NiMn]	[NiMn] [−]	[NiHMn]	[Ni(H ₂)Mn] ⁺	[NiMn] ⁺	[NiHMn] [−]	[Ni(H ₂)Mn]
Ni–Mn	0.112	0.211	0.301	0.353	0.226	0.278	0.355	0.259
Mn–OH ₂	0.198							
Mn–H				0.486	0.288, 0.272		0.443	0.313, 0.238
Ni–H				0.291	0.096, 0.044		0.388	0.220, 0.074
H–H					0.534			0.474
Mn–S _{ab}	0.711	0.671	0.685	0.639	0.680	0.763	0.653	0.682
Ni–S _{ab}	1.103	1.081	0.824	1.067	1.077	1.104	0.769	0.830
Ni–S _{cd}	0.980	0.908	0.778	0.893	0.916	0.934	0.733	0.734
Mn–C	1.194, 1.285	1.287, 1.212	1.295, 1.234	1.274, 1.193	1.165, 1.138	1.163, 1.254	1.309, 1.245	1.205, 1.160
C–O	2.463, 2.405	2.310, 2.310	2.301, 2.295	2.343, 2.352	2.459, 2.541	2.483, 2.413	2.287, 2.280	2.402, 2.456

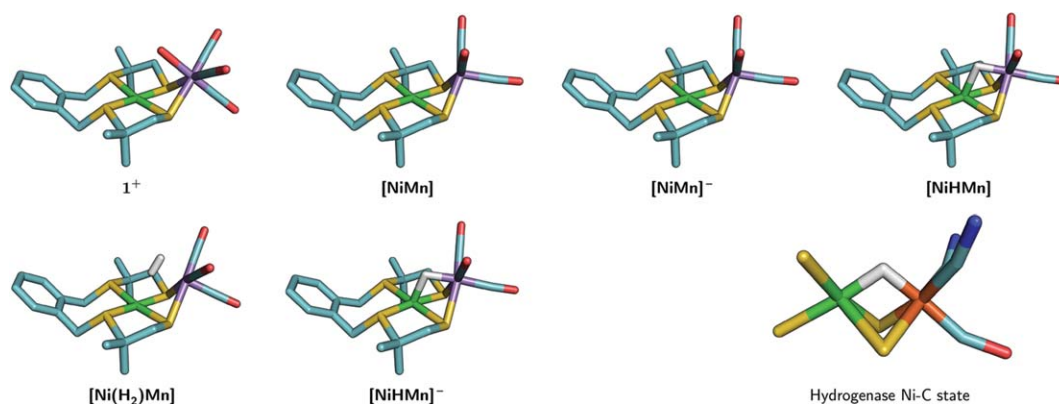


Fig. 6 DFT optimized structures of the intermediates for H_2 evolution catalyzed by $[\text{NiMn}]^+$ along with the structure of the Ni-C state of NiFe hydrogenases. Color code: H (white), C (cyan), O (red), S (yellow), Mn (purple), Ni (green), N (blue) and Fe (orange).

The homolytic process involves a step which is second-order in terms of the catalyst concentration. By contrast the heterolytic mechanism only involves steps which are first-order with respect to both proton and catalyst concentrations. In a first phase we checked if one such step is rate-determining, by examining the dependence of η on the acid and catalyst concentrations.

Fig. 7 plots η as a function of the ratio of acid to catalyst concentrations, β , for two different values of the scan rate and two different catalyst concentrations. The average values of η for each scan rate are shown as lines and regions with deviations of $\pm 7.5\%$ around the average are shaded. It is clear from the figure that all experimental points for a given scan rate lie within the shaded regions. As these data points were obtained with different concentrations of catalyst (1 and 5 mmol L^{-1}) and acid (deducible from β and the catalyst concentration), it means that the catalytic efficiency, and hence the reaction kinetics, depends on neither the catalyst concentration nor the acid concentration

independently, but only on their ratio. Thus neither a protonation step nor a bimolecular reaction between two catalysts is rate-determining for catalysis.

To obtain quantitative kinetic data and to discriminate between homolytic and heterolytic H_2 -evolution steps, we simulated the full catalytic cycles using a program developed in-house.

Simulations with a homolytic mechanism. We ran a large number of simulations for the homolytic mechanism shown below (AH stands for trifluoroacetic acid):

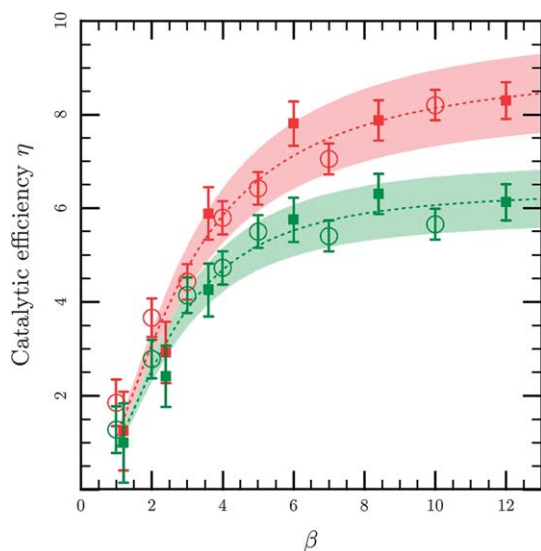
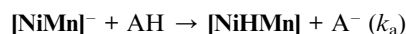
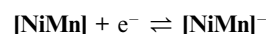


Fig. 7 Catalytic efficiency η as a function of β ([acid]/[catalyst]) for different values of the scan rate (red 100 mV s^{-1} and green 30 mV s^{-1}) and of catalyst concentration (filled squares: 1 mmol L^{-1} , empty circles 5 mmol L^{-1}). The dotted lines denote the average efficiency whereas the shaded areas indicate the regions with deviations of $\pm 7.5\%$ around the average.

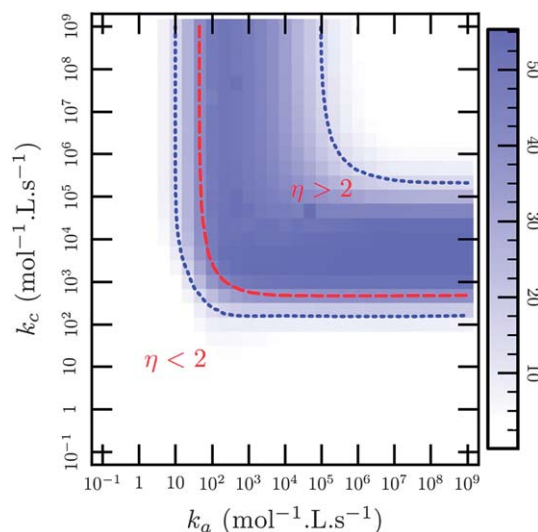


Fig. 8 Map of the percentage deviation from the mean catalytic efficiency as a function of k_a and k_c . Each square on the map corresponds to a series of simulations with catalyst concentrations of 1 and 5 mmol L^{-1} and a value of β ranging from 0 to 15 (as in Fig. 7). The dotted blue lines stand for $\pm 7.5\%$ deviation and the dashed red line delimits the regions of the plane where the catalytic efficiency is greater or less than 2 (as indicated).



The parameters introduced in the simulation were: (i) the catalyst concentration (1 and 5 mmol L⁻¹); (ii) the β value (varied from 0 to 15); and (iii) the bimolecular catalytic rate constants (k_a for the protonation and k_c for the bimolecular reductive elimination step). The scan rate was kept constant (100 mV s⁻¹) in all the simulations. We computed the catalytic efficiency η for each of the conditions and plotted it against β for each pair of values of the catalytic rate constants (k_a , k_c) as in Fig. 7. From such plots, we were able to compute the percentage deviation of simulated points from the average dependence on β . This percentage deviation is plotted as a function of k_a and k_c in Fig. 8.

In order to reproduce the experimental data shown in Fig. 7, the pair of values (k_a , k_c) relevant to the actual catalytic mechanism must lie in regions within which the percentage deviation is less than $\pm 7.5\%$ about the average (the shaded regions in Fig. 7). These are the areas shown in white in Fig. 8. In addition, the catalytic efficiency should be greater than, say, 2 which corresponds to the upper-right part of Fig. 8 delimited by the dotted red line. This means that, for a homolytic mechanism to reproduce the data in Fig. 7, one would need to have a homolytic rate-constant k_c of at least 3.10^5 mol L⁻¹ s⁻¹. However, even in the upper-right part of Fig. 8, the homolytic mechanism fails to reproduce the dependence of η upon β (this situation is called total catalysis since the catalytic process is limited only by mass transport of the acid to the electrode^{43,44}), whereas we observe a plateau in the catalytic rate for β values greater than 6. Thus homolytic H₂ evolution seems unlikely.

Simulations with a heterolytic mechanism. The same approach as above was employed to simulate the electrocatalytic data for a heterolytic mechanism. We considered the catalytic sequence shown in Fig. 9 based upon the results of our DFT calculations.

From the data shown in Fig. 7, we extracted three parameters: (i) η_{max} (8.5 ± 0.5 at 100 mV s⁻¹), the plateau value of η , (ii) $\beta_{1/2}$ (2.5 ± 0.5 at 100 mV s⁻¹), the value of β for which η is half its maximum value η_{max} ; and (iii) the percentage deviation about the average η ($\pm 7.5\%$) within which all experimental points lie. We

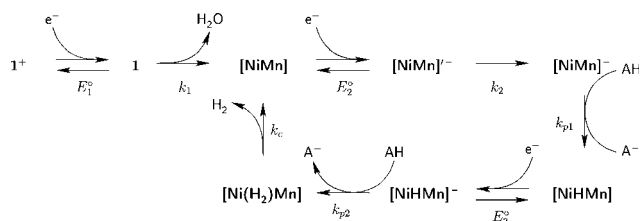


Fig. 9 Simulated electrocatalytic pathway for heterolytic hydrogen evolution catalyzed by $[\text{NiMn}]^+$. As in Table 2, $[\text{NiMn}]^{\bullet-}$ is the species obtained after reduction of $[\text{NiMn}]$ but before the structural rearrangement that gives rise to electrochemical irreversibility. k_1 and k_2 are the rate constants of the chemical reactions that follow the first and the second reductions, respectively. k_{p1} and k_{p2} are bimolecular protonation rate constants and k_c is the rate constant for release of H₂ (AH stands for trifluoroacetic acid).

ran a number of simulations for the mechanism shown in Fig. 9, using a protocol similar to that used for obtaining the data shown in Fig. 8. In addition to the E_1^0 , k_1 and E_2^0 , k_2 parameters that define the electrochemical response in the absence of acid, there are four parameters that characterize the steps involved in catalysis: the two protonation rate constants k_{p1} and k_{p2} , the potential of the $[\text{NiHMn}]/[\text{NiHMn}]^{\bullet-}$ couple, E_3^0 , and k_c the rate constant for release of H₂ from $[\text{Ni}(\text{H}_2)\text{Mn}]$. Following the results of the DFT computations, we assumed E_3^0 to be equal to E_2^0 .⁴⁵ As far as the protonation rate constants are concerned, DFT computations (Table 2) show that the first protonation step has more driving force than the second one, which means that $k_{p1}/k_{p2} \geq 1$. This left three free parameters: k_{p2} , k_c and k_{p1}/k_{p2} . Simulations were performed for catalyst concentrations of 1 and 5 mmol L⁻¹, β values ranging from 0 to 15, values of k_{p2} ranging from 10 mol L⁻¹ s⁻¹ to 10⁸ mol L⁻¹ s⁻¹, values of k_c ranging from 1 to 10⁷, and values of the ratio k_{p2}/k_{p1} ranging from 1 to 1000.

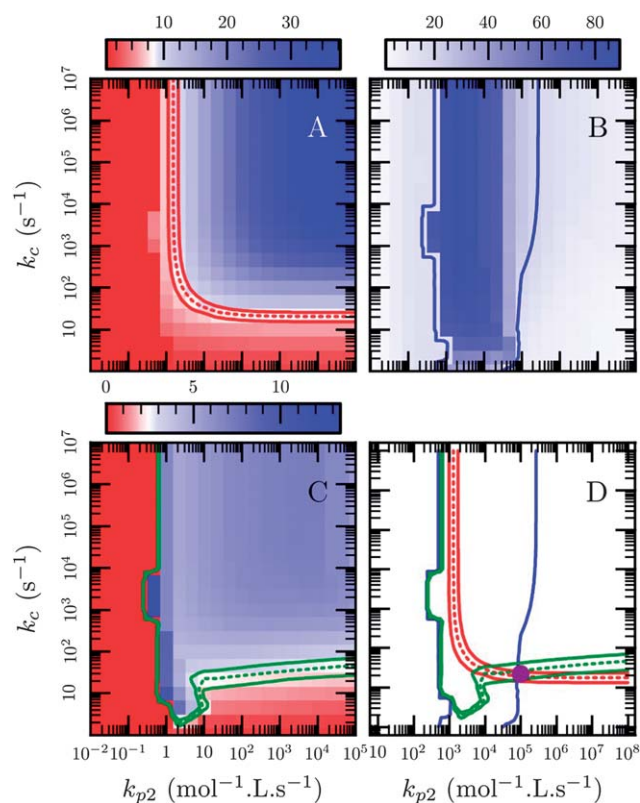


Fig. 10 Results of the cyclic voltammogram simulations, for a ratio $k_{p1}/k_{p2} = 1$. Each square represents a series of simulations for a given k_{p2} and k_c with 1 and 5 mmol L⁻¹ as catalyst concentrations and the β ratio varying from 0 to 15. Squares are in white if the calculated parameter value corresponds to the experimental one within the experimental error range, in red if it is lower and in blue if it is higher. Panel A shows the calculated values of η_{max} , panel B the percentage deviation and panel C $\beta_{1/2}$. The lines on the panels are isocontour lines for particular parameter values. These are: $\eta_{\text{max}} = 8$ (red solid), 8.5 (red dotted) and 9 (red solid); a percentage deviation of $\pm 7.5\%$ (blue solid); and $\beta_{1/2} = 2$ (green solid), 2.5 (green dotted) and 3 (green solid). Panel D shows uniquely the isocontours, and hence can be used to determine the region of (k_{p2} , k_c) space where the characteristics of the simulated $\eta = f(\beta)$ curves match those of the experimental ones: this is the region outside of the blue lines and within the red and green lines.

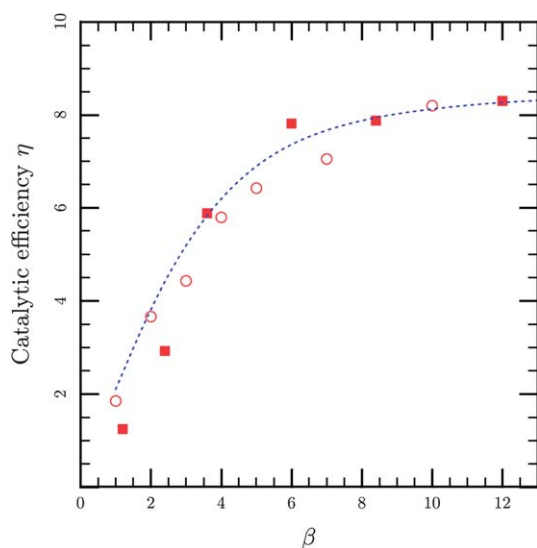


Fig. 11 Experimental and simulated catalytic efficiencies at 100 mV s^{-1} and two different catalyst concentrations (filled squares: 1 mmol L^{-1} , empty circles 5 mmol L^{-1}). Simulation parameters are $k_{p1} = k_{p2} = 10^5 \text{ mol}^{-1} \text{ L s}^{-1}$, $k_c = 21 \text{ s}^{-1}$.

We computed the amplitude of the catalytic wave and the resulting catalytic efficiency for each simulated voltammogram, built $\eta = f(\beta)$ curves for each set of parameters (k_{p2} , k_c , k_{p1}/k_{p2}) and determined the three aforementioned parameters (η_{max} , $\beta_{1/2}$ and maximum percentage deviation) from them. The results are presented in Fig. 10 for $k_{p1}/k_{p2} = 1$.

The regions of parameter space within which the simulated values of η_{max} , $\beta_{1/2}$ and maximum percentage deviation match the experimental values are relatively narrow and the region in which all three match is very narrow indeed. This is marked as a purple dot on Fig. 10D and corresponds to parameter values of $5 \times 10^4 \leq k_{p2} = k_{p1} \leq 10^6 \text{ mol}^{-1} \text{ L s}^{-1}$, $k_c = 21 \pm 3 \text{ s}^{-1}$. Fig. 11 shows that for parameter values in this range there is a very good agreement between the simulated $\eta = f(\beta)$ curve and the experimental one. Increasing the k_{p1}/k_{p2} ratio slightly shifts the region where $\beta_{1/2}$ matches the experimental values (see ESI†) and does not affect η_{max} and the percentage deviation.

3. Discussion

Our results indicate that the nickel–manganese compound **1**⁺ acts as a low molecular weight model of the active site of NiFe hydrogenases from both a structural and a functional point of view.

As far as structural features are concerned, our modelling correctly accounts for the contraction of the distance between the two metals observed in the reduced forms of the enzymes as compared to the more oxidized states.⁴⁶ Second, our results also clearly show that the hydride ligand in **[NiHMn]** and **[NiHMn][−]** (Fig. 6) is stabilized in a bridging dissymmetric configuration between nickel and manganese. We observed similar structures in our calculations of Ni–Ru^{16,17} and Ni–Fe¹⁸ compounds. This configuration can be compared with the structure of the reduced Ni–C state of **[NiFe]** hydrogenases obtained by HYSORE measurements (Fig. 6), in which a bridging site between the metals is occupied by a hydride ligand.^{47,48} In the natural

[Ni^{III}(μ-H)Fe^{II}] centre, the Ni–H bond is, however, significantly shorter (1.61 \AA) as compared to that in **[NiHMn]** (1.93 \AA) whereas the Fe–H distance (1.72 \AA) is longer than that of Mn–H (1.63 \AA). The dissymmetry is, however, much lower in the reduced hydride derivative **[NiHMn][−]** (1.76 \AA for Ni–H and 1.66 \AA for Mn–H). The calculated charge on the hydridic hydrogen atom for the two species (-0.22 for **[NiHMn]**; 0.32 for **[NiHMn][−]**) is significantly higher than those determined from similar calculations on the Ni–C (-0.01) and Ni–R (-0.06) states of NiFe hydrogenases respectively,^{49,50} probably because of the difference in the bridging mode and of charge less delocalized on the sulfur ligands in the mimic. Protonation of both hydride species yields dihydrogen complexes with a peculiar H_2 coordination mode with regard to both Mn (side-on η^2 -coordination) and nickel (end-on coordination). A similar structure has been proposed by Hall *et al.* for the Ni–R state of NiFe hydrogenases on the basis of DFT calculations.⁵¹ In addition, the H–H distance in both **[Ni(H₂)Mn]⁺** (0.84 \AA) and **[Ni(H₂)Mn]** (0.87 \AA) is in the lower range for a “true” dihydrogen complex ($0.8\text{--}1.0 \text{ \AA}$),³⁵ in good agreement with the low enthalpies of H_2 binding. Similarly hydrogen evolution from the Ni–R form of NiFe hydrogenases occurs spontaneously under mild conditions.

A second very important similarity of NiFe hydrogenases and the Ni–Mn mimic reported here is that both produce H_2 in a heterolytic way. DFT calculations and systematic screening, based on electrochemical simulations, of a large number of parameters for homolytic and heterolytic mechanisms discard the possibility that two hydride intermediates react together and eliminate H_2 for the following reasons: (i) from DFT-calculated enthalpies such bimolecular reductive eliminations are very endothermic; (ii) simulations show that a homolytic recombination rate constant higher than $3 \times 10^5 \text{ mol L}^{-1} \text{ s}^{-1}$ is required to match the experimental percentage deviation. This is at least one order of magnitude higher than that measured for **[HCo(dmgH)(dmgH₂)(PBU₃)]⁺** ($1.7 \times 10^4 \text{ mol L}^{-1} \text{ s}^{-1}$)⁵² which is one of the highest reported in the literature; and (iii) even with such a high rate constant, the dependence of the catalytic efficiency with β is not consistent with the experimental data. By contrast we were able to fully reproduce the experimental catalytic efficiency using a heterolytic mechanism from the reduced hydride derivative **[NiHMn][−]**. A similar behaviour has long been proposed for similar Ni–Ru mimics but has not been conclusively demonstrated.^{16,17} The design of catalytic systems functioning through a heterolytic pathway is indeed a prerequisite for technological applications that will require immobilization of the catalyst onto an electrode substrate since in this case protonation of hydride sites at the surface can proceed smoothly. In contrast, systems evolving H_2 through a homolytic and thus bimolecular pathways should be inefficient when grafted onto an electrode since two different immobilized centres will not be able to react together.^{53,54} The rate-determining step for H_2 evolution catalyzed by **1**⁺ appears to be rather slow (20 s^{-1}) when compared to the turnover frequency of native hydrogenases ($1500\text{--}9000 \text{ s}^{-1}$) or to the best bio-inspired mononuclear catalysts designed so far and that also evolve H_2 heterolytically (350 s^{-1}).¹⁰ However, **1**⁺ displays a catalytic efficiency of the same order of magnitude as that of other Ni–Fe dinuclear mimics.^{18–20}

Despite the quite high degree of structural similarity with the active site of NiFe hydrogenases, H_2 is evolved at the cost of

a high overpotential when catalyzed by this new Ni–Mn mimic. Given the accuracy of the methodology used (about 40 mV), the overpotential requirement (about 860 mV) for H₂ evolution catalyzed by **1Br** compares well to that (840 mV) recalculated with the same method^{30,55} for the recently described Ni–Fe mimic of hydrogenase [Ni(xbsms)FeCp(CO)]⁺.¹⁸ Such high overpotential requirements have also been determined with Ni–Ru^{15,17,26,27} models. This strongly limits the practical application of these synthetic catalysts. One reason for a high overpotential may be due to the clear difference in the redox states of the metals in these dinuclear catalysts as compared to the redox states of the active site of the enzyme. First, both the Ni and Mn centres in the model compound experience changes in oxidation state along the cycle. Similar electronic changes were observed on both metal centres in Ni–Ru¹⁶ and Ni–Fe¹⁸ mimics. This contrasts with the observation that the iron cyanocarbonyl moiety is not redox active in the active site of NiFe hydrogenases. Thus neither [NiHMn] with a Ni^{II}–Mn^I structure and Mn^I isoelectronic to Fe^{II}, nor [NiHMn][–] (Ni^I–Mn^I), are relevant mimics of the Ni^{III}–Fe^{II} Ni–C state.⁴⁸ Second, the spin densities on the coordinating sulfur atoms are quite small (Tables 3 and S3†) whereas both EPR/ENDOR experiments and quantum chemical studies of the active site of NiFe hydrogenases show that significant spin populations are located on the sulfur atoms.^{49,50,56}

We believe that all these differences in the electronic structures of the mimics incorporating the [Ni(xbsms)] moiety as compared to that of the enzyme are linked at least partly to the square planar configuration found at the Ni centre. This strongly stabilizes the Ni^{II} state with regards to both oxidation and reduction. Hence, the first reductive process does not occur at Ni as in the enzyme but at the organometallic moiety, whatever its nature and metal content (Ru, Fe, Mn). Thus a better mimicry should consider ligands that prevent the Ni centre from adopting such a stable configuration.

4. Conclusion

The nickel–manganese compound reported here is a new mimic of the active site of NiFe hydrogenases that does not contain any noble metal. It displays a catalytic activity for hydrogen evolution with overpotential requirement, turnover frequency and stability similar to the Ni–Fe mimics recently reported.^{18–20} Thanks to DFT analysis and systematic simulation of the electrocatalytic data, we find that this complex mediates hydrogen evolution in a heterolytic fashion from a bridging hydride intermediate with a structure similar to that of the Ni–C active state of NiFe hydrogenases. Further modifications of the nickel and manganese coordination spheres are likely to improve catalytic performances so as to provide a valuable alternative to the use of noble metals as electrocatalysts for hydrogen production.

Experimental section

Materials

All reactions were routinely performed under an inert atmosphere of argon using standard Schlenk techniques. Diethyl ether was distilled by refluxing over Na/benzophenone and distilled under argon. NMR solvents (Eurisotop) were deoxygenated by

three freeze–pump–thaw cycles and stored over molecular sieves. Commercial dimethylformamide for electrochemistry was degassed by bubbling nitrogen through it. [Ni(xbsms)] was prepared according to a previously reported procedure.²² [Mn(CO)5Br] was purchased from Strem Chemicals and used without further purification. The supporting electrolyte (*n*-Bu₄N)BF₄ was prepared from (*n*-Bu₄N)HSO₄ (Aldrich) and NaBF₄ (Aldrich) and dried overnight at 80 °C under vacuum. Trifluoroacetic acid (TFA, Sigma) was used as received.

Methods and instrumentation

NMR spectra were recorded at room temperature in 5 mm tubes on a Bruker AC 300 spectrometer equipped with a QNP probehead, operating at 300.0 MHz for ¹H. Solvent peaks are used as internal references relative to Me₄Si for ¹H and ¹³C chemical shifts (listed in ppm). ESI mass spectra were recorded with a Finnigan LCQ thermoquest ion-trap. Elemental analyses were performed by the “Service Central d’Analyse du CNRS” (Vernaison, France). All electrochemical measurements were carried out under nitrogen at room temperature. A standard three-electrode configuration was used consisting of a glassy carbon (3 mm in diameter) or platinum (2 mm in diameter) disk as the working electrode, an auxiliary platinum wire and an Ag/AgCl/aqueous AgCl_{sat} + KCl 3 M (denoted as Ag/AgCl throughout this text) reference electrode closed by a Vycor frit and dipped directly into the solution. In order to take into account the liquid junction potential between aqueous and non-aqueous solution, the electrode was systematically calibrated with ferrocene after each experiment. The potential of the Fc⁺/Fc couple was found to be 0.53 V vs. Ag/AgCl in DMF. The Fc⁺/Fc couple (*E*₀ = 0.400 V vs. SHE)⁵⁷ can be used to quote potentials relative to a SHE, when needed. Cyclic voltammograms were recorded with a EG&G PAR 273A instrument. Solution concentrations were approximately 1 mM for the catalyst and 0.1 M for the supporting electrolyte (*n*-Bu₄N)BF₄. Electrodes were polished with an MD-Nap polishing pad with 1 μm monocrystalline diamond DP suspension and DP lubricant blue (Struers). Additions of TFA were made by syringe as a 0.12 mol L^{–1} solution in dimethylformamide. Blank cyclic voltammograms of the supporting electrolyte and of TFA in DMF are given in the ESI†. Bulk electrolysis experiments and coulometry were carried out on an EG&G PAR 273A instrument in dimethylformamide, using a mercury pool cathode. The platinum-grid counter electrode was placed in a separate compartment connected by a glass-frit and filled with a 0.1 M solution of (*n*-Bu₄N)BF₄ in degassed dimethylformamide. A previously described made-to-measure electrolysis cell with a cylindrical reservoir was used.^{15,17} The following procedure was followed for catalytic acid reduction bulk electrolysis: a degassed DMF solution (7 mL) containing 0.1 M (*n*-Bu₄N)BF₄ and TFA (0.1 M) was first electrolyzed at –1.3 V vs. Ag/AgCl until the current reached 1% of its initial value. The catalyst (1 mM) was then added and electrolysis was performed at the same potential with coulometric monitoring. In parallel, the volume of H₂ evolved was measured at atmospheric pressure. Hydrogen was tested for purity using a Delsi Nermag DN200 GC chromatograph equipped with a 3 m Porapack column and a thermal conductivity detector (TCD). Nitrogen under 1 bar was used as the carrier gas. The whole apparatus was

thermostatted at 45 °C. Under these conditions, pure hydrogen has an elution time of 77 s.

Cyclic voltammograms were simulated using an in-house program implementing the FIFD solver described by Rudolph,⁵⁸ including his method for solving non-linear equations.⁵⁹ Experimental voltammograms were analyzed using Soas.⁶⁰ Contour plots were drawn using Tioga's make contour function (see <http://tioga.rubyforge.org>) that in turns uses the contouring algorithm from Gri (<http://gri.sourceforge.net>). Plots were drawn using ctioga2 (<http://ctioga2.rubyforge.org>).

Synthesis of [Ni(xbsms)Mn(H₂O)(CO)₃]Br ([NiMn]Br)

A suspension of [Ni(xbsms)] (66 mg, 0.164 mmol) and [Mn(CO)₅]Br (45 mg, 0.164 mmol) in Et₂O (25 mL) was stirred in the dark for 4 days. The red solid is collected by filtration, washed with Et₂O (5 mL) and dried under vacuum (90 mg, 86%). ¹H NMR (CD₂Cl₂): δ 7.30 (d, 2H, Ar), 7.22 (d, 2H, Ar), 5.54 (d, 2H, *J*_{AB} = 12 Hz, ArCH₂S), 3.51 (d, 2H, *J*_{AB} = 12 Hz, ArCH₂S), 3.27 (d, 2H, *J*_{AB} = 12.6 Hz, (CH₃)₂CCH₂S), 2.05 (d, 2H, *J*_{AB} = 12.6 Hz, (CH₃)₂CCH₂S), 1.74 (s, 6H, Me), 1.52 (s, 6H, Me). IR (CH₂Cl₂): ν_{CO} = 2018 (vs.), 1929 (m, br) and 1911 cm⁻¹. ESI-MS: *m/z* (%) 541 (100) {[M] – H₂O}⁺. Elemental analysis calculated for C₁₉BrH₂₄MnNiO₃S₄·H₂O (640.20): C 35.65; Br 12.48; H 4.09; Mn 8.58; Ni 9.17; S 20.03. Found: C 36.51; Br 12.54; H 3.99; Mn 8.43; Ni 8.80; S 19.61%.

Properties of trifluoroacetic acid in DMF

Simulations required a value for the diffusion coefficient of trifluoroacetic acid in DMF. We took advantage of the fact that the reduction of TFA is reversible at a platinum electrode in DMF (see ESI†) to obtain both the diffusion coefficient *D* (3.4 ± 0.4 cm² s⁻¹) and its p*K*_a (6.0 ± 0.3).

Computational details

DFT calculations were performed with the Jaguar quantum chemistry program (version 5.2).⁶¹ Calculations were carried out with two different functionals, B3LYP and BP86, and the LACV3P**++ basis set, which is of triple-zeta quality and has polarization and diffuse functions. For each modelled species in the catalytic cycle, geometry optimizations were carried out first in the gas-phase followed by optimization with an implicit solvent model (Poisson–Boltzmann solver) corresponding to DMF.

Redox potentials and p*K*_a values were calculated in the standard fashion as previously described.^{16,17} The p*K*_a value for TFA in DMF was determined to be 4.6 (B3LYP) and 4.1 (BP86) and the absolute half-cell potential for the Fc/Fc⁺ couple was calculated to be in the range –4.64 (BP86) and –5.36 (B3LYP) compared to the –5.05 eV value that is measured experimentally.

Acknowledgements

The authors thank Colette Lebrun for ESI-MS analysis. This work was supported by the Technological Research Division of CEA (pH₂oton project), the Life Science Division of CEA (Biohydrogen program) and the French National Research Agency (ANR, Grant 07-BLAN0298-01 and Carnot funding).

Notes and references

- W. Vielstich, A. Lamm and H. A. Gasteiger, *Handbook of Fuel Cells: Fundamentals, Technology and Applications*, Wiley, Chichester, UK, Hoboken, NJ, 2003.
- R. B. Gordon, M. Bertram and T. E. Graedel, *Proc. Natl. Acad. Sci. U. S. A.*, 2006, **103**, 1209–1214.
- J. C. Fontecilla-Camps, A. Volbeda, C. Cavazza and Y. Nicolet, *Chem. Rev.*, 2007, **107**, 4273–4303.
- A. Le Goff, V. Artero, B. Jousset, P. D. Tran, N. Guillet, R. Metaye, A. Fihri, S. Palacin and M. Fontecave, *Science*, 2009, **326**, 1384–1387.
- P. D. Tran, V. Artero and M. Fontecave, *Energy Environ. Sci.*, 2010, **3**, 727–747.
- P. D. Tran, A. Le Goff, J. Heidkamp, B. Jousset, N. Guillet, S. Palacin, H. Dau, M. Fontecave and V. Artero, *Angew. Chem., Int. Ed.*, 2010, DOI: 10.1002/anie.201005427.
- M. R. DuBois and D. L. DuBois, *Chem. Soc. Rev.*, 2009, **38**, 62–72.
- M. Rakowski Dubois and D. L. Dubois, *Acc. Chem. Res.*, 2009, **42**, 1974–1982.
- A. D. Wilson, R. H. Newell, M. J. McNevin, J. T. Muckerman, M. R. DuBois and D. L. DuBois, *J. Am. Chem. Soc.*, 2006, **128**, 358–366.
- A. D. Wilson, R. K. Shoemaker, A. Miedaner, J. T. Muckerman, D. L. DuBois and M. R. DuBois, *Proc. Natl. Acad. Sci. U. S. A.*, 2007, **104**, 6951–6956.
- J. F. Capon, F. Gloaguen, F. Y. Petillon, P. Schollhammer and J. Talarmin, *Coord. Chem. Rev.*, 2009, **253**, 1476–1494.
- C. Tard and C. J. Pickett, *Chem. Rev.*, 2009, **109**, 2245–2274.
- S. Canaguier, V. Artero and M. Fontecave, *Dalton Trans.*, 2008, 315–325.
- T. Matsumoto, B. Kure and S. Ogo, *Chem. Lett.*, 2008, **37**, 970–971.
- Y. Oudart, V. Artero, J. Pécaut, C. Lebrun and M. Fontecave, *Eur. J. Inorg. Chem.*, 2007, 2613–2626.
- L. Vaccaro, V. Artero, S. Canaguier, M. Fontecave and M. J. Field, *Dalton Trans.*, 2010, **39**, 3043–3049.
- S. Canaguier, L. Vaccaro, V. Artero, R. Ostermann, J. Pécaut, M. J. Field and M. Fontecave, *Chem.–Eur. J.*, 2009, **15**, 9350–9365.
- S. Canaguier, M. Field, Y. Oudart, J. Pécaut, M. Fontecave and V. Artero, *Chem. Commun.*, 2010, **46**, 5876–5878.
- B. E. Barton, C. M. Whaley, T. B. Rauchfuss and D. L. Gray, *J. Am. Chem. Soc.*, 2009, **131**, 6942–6943.
- B. E. Barton and T. B. Rauchfuss, *J. Am. Chem. Soc.*, 2010, **132**, 14877–14885.
- R. Hoffmann, *Angew. Chem., Int. Ed.*, 1982, **21**, 711–724.
- J. A. W. Verhagen, D. D. Ellis, M. Lutz, A. L. Spek and E. Bouwman, *Dalton Trans.*, 2002, 1275–1280.
- M. Razavet, V. Artero, C. Cavazza, Y. Oudart, C. Lebrun, J. C. Fontecilla-Camps and M. Fontecave, *Chem. Commun.*, 2007, 2805–2807.
- U. Prinz, U. Koelle, S. Ulrich, A. E. Merbach, O. Maas and K. Hegetschweiler, *Inorg. Chem.*, 2004, **43**, 2387–2391.
- This hypothesis is further supported by our DFT calculations of these related complexes (see below).
- Y. Oudart, V. Artero, J. Pécaut and M. Fontecave, *Inorg. Chem.*, 2006, **45**, 4334–4336.
- Y. Oudart, V. Artero, L. Norel, C. Train, J. Pécaut and M. Fontecave, *J. Organomet. Chem.*, 2009, **694**, 2866–2869.
- C. H. Lai, J. H. Reibenspies and M. Y. Darensbourg, *Angew. Chem., Int. Ed.*, 1996, **35**, 2390–2393.
- R. S. Nicholson and I. Shain, *Anal. Chem.*, 1964, **36**, 706–723.
- V. Fourmond, P.-A. Jacques, M. Fontecave and V. Artero, *Inorg. Chem.*, 2010, **49**, 10338–10347.
- J. A. Widegren and R. G. Finke, *J. Mol. Catal. A: Chem.*, 2003, **198**, 317–341.
- We checked that [Mn(CO)₃(acetone)₃]Otf does not display any catalytic activity for TFA reduction in DMF at a glassy carbon electrode.
- DFT calculations also show that such a change in the isomeric form has no further effect regarding the catalytic cycle.
- L. E. Roy, E. Jakubikova, M. G. Guthrie and E. R. Batista, *J. Phys. Chem. A*, 2009, **113**, 6745–6750.
- G. J. Kubas, *Chem. Rev.*, 2007, **107**, 4152–4205.
- M. Besora, A. Lledos and F. Maseras, *Chem. Soc. Rev.*, 2009, **38**, 957–966.

- 37 N. V. Belkova, L. M. Epstein and E. S. Shubina, *Eur. J. Inorg. Chem.*, 2010, 3555–3565.
- 38 P. E. M. Siegbahn, J. W. Tye and M. B. Hall, *Chem. Rev.*, 2007, **107**, 4414–4435.
- 39 C. Bourdillon, C. Demaille, J. Moiroux and J. M. Saveant, *J. Am. Chem. Soc.*, 1993, **115**, 2–10.
- 40 V. Proux-Delrouyre, C. Demaille, W. Leibl, P. Setif, H. Bottin and C. Bourdillon, *J. Am. Chem. Soc.*, 2003, **125**, 13686–13692.
- 41 V. Fourmond, B. Lagoutte, P. Setif, W. Leibl and C. Demaille, *J. Am. Chem. Soc.*, 2007, **129**, 9201–9209.
- 42 We have chosen the first wave as the experimental determination of its amplitude is more accurate.
- 43 C. P. Andrieux, C. Blocman, J. M. Dumasbouchiat, F. Mhalla and J. M. Saveant, *J. Electroanal. Chem.*, 1980, **113**, 19–40.
- 44 J. M. Saveant and K. B. Su, *J. Electroanal. Chem.*, 1984, **171**, 341–349.
- 45 The exact value of E_3^0 has limited impact on the catalytic response, provided that it is not lower than -2.0 V vs. Fc^+/Fc , in which case simulations show that the catalytic process occurs on a third wave at lower potential.
- 46 W. F. Zhu, A. C. Marr, Q. Wang, F. Neese, D. J. E. Spencer, A. J. Blake, P. A. Cooke, C. Wilson and M. Schroder, *Proc. Natl. Acad. Sci. U. S. A.*, 2005, **102**, 18280–18285.
- 47 M. Brecht, M. van Gastel, T. Buhrke, B. Friedrich and W. Lubitz, *J. Am. Chem. Soc.*, 2003, **125**, 13075–13083.
- 48 W. Lubitz, E. Reijerse and M. van Gastel, *Chem. Rev.*, 2007, **107**, 4331–4365.
- 49 L. De Gioia, P. Fantucci, B. Guigliarelli and P. Bertrand, *Inorg. Chem.*, 1999, **38**, 2658–2662.
- 50 P. Amara, A. Volbeda, J. C. Fontecilla-Camps and M. J. Field, *J. Am. Chem. Soc.*, 1999, **121**, 4468–4477.
- 51 S. Q. Niu, L. M. Thomson and M. B. Hall, *J. Am. Chem. Soc.*, 1999, **121**, 4000–4007.
- 52 T. H. Chao and J. H. Espenson, *J. Am. Chem. Soc.*, 1978, **100**, 129–133.
- 53 L. A. Berben and J. C. Peters, *Chem. Commun.*, 2010, **46**, 398–400.
- 54 V. Artero and M. Fontecave, *Coord. Chem. Rev.*, 2005, **249**, 1518–1535.
- 55 The half-wave potential of the catalytic wave is -1.81 V vs. Fc^+/Fc for a 10 mmol L^{-1} concentration of TFA in DMF.
- 56 L. De Gioia, P. Fantucci, B. Guigliarelli and P. Bertrand, *Int. J. Quantum Chem.*, 1999, **73**, 187–195.
- 57 H. M. Koepp, H. Wedt and H. Strehlow, *Z. Elektrochem.*, 1960, **64**, 483.
- 58 M. Rudolph, *J. Electroanal. Chem.*, 1991, **314**, 13–22.
- 59 M. Rudolph, *J. Electroanal. Chem.*, 1992, **338**, 85–98.
- 60 V. Fourmond, K. Hoke, H. A. Heering, C. Baffert, F. Leroux, P. Bertrand and C. Leger, *Bioelectrochemistry*, 2009, **76**, 141–147.
- 61 *Jaguar 5.2*, Schrödinger L.L.C., Portland, OR, 2003.